

IPGP/CEA-LETI/CIRES-NOAA DGRF 2020 candidate model for IGRF-14

This note is to provide the information requested to accompany the DGRF 2020 candidate model that our IPGP-led team wishes to submit for consideration for IGRF-14.

1) Team

Lead Institution: Université Paris Cité, Institut de Physique du Globe de Paris (IPGP)

Participating Institutions: CEA-LETI, Grenoble, France; CIRES, University of Colorado, Boulder, CO, USA; NOAA National Centers for Environmental Information, Boulder, CO, USA.

Co-Team leaders: G. Hulot (IPGP), L. Chauvet (IPGP)

Team members: R. Deborde (IPGP), Jean-Michel Léger (CEA-LETI), Thomas Jager (CEA-LETI), M. Fillion (CIRES, NOAA), P. Coisson (IPGP)

2) Data used

Data type and version: Only data collected by the Alpha and Bravo satellites from the ESA Swarm mission have been used. The source magnetic data are the ASM-V data produced by the ASM instruments running in vector mode (see Léger et al., 2015), processed within IPGP using L0 data version 0201, v9 version software (developed by CEA-LETI) to produce L1a data, XPh1B software to produce L1b data with UTC time stamps, as well as stray field corrections (now also including dBSun corrections for consistency with L1b nominal data version 0602/0606) from 0602/0605 nominal ASMxAUX, and updated CCDB with optimized gains (1.22 for Alpha, 1.27 for Bravo, as provided by CEA-LETI on 23/04/18). This calibration procedure is the one described in Vigneron et al. (2021). All the ASM-V data used are expressed in the reference frame of the ASM instruments. Attitude information is recovered using the q_NE_CFR quaternion information from 0602/0606 MAGxLR files, also used to recover satellite positions (radius/lat/long). Note that Euler angles defining the rotation between the ASM and STR CRF reference frames are therefore jointly computed with the models (see below).

Data temporal distribution: First data used is from 26/03/2014, last data used is from 31/07/2024 (124 months). Note that we did not use the first few months of available ASM-V data in 2013 and 2014, nor the latest (after July 2024), as this was not deemed necessary to derive a DGRF candidate model for epoch 01/01/2020

Data selection: Data selection criteria are identical (except for possible thresholds when using indices, see below) to those previously used in Vigneron et al. (2021) and Hulot et al. (2015), where details can be found. These can be summarized in the following way:

- Only night-side data are used
- Magnetically quiet conditions (based on $RC < 2\text{nT/h}$ and $K_p < 2+$) are required
- For all (absolute) QD latitudes above 55° , only scalar data have been used, also requesting that $E_{m,12} < 0.8 \text{ mV/m}$
- For all other QD latitudes, only vector data have been used, unless the scalar residual (difference between scalar and modulus of vector) is larger than 0.3 nT , or the piezoelectric motor has been activated within 3s of the data measurement (since this may produce artifacts, see Léger et al., 2015), in which case only the scalar data is considered.
- A final decimation is being used to avoid over-representation along tracks (amounting to separate data by about 30s)

Again as in Hulot et al. (2015) and Vigneron et al. (2021), a mild additional selection criteria was finally introduced to ensure that a meaningful (non-spurious) L1b nominal data version 0602/0606 (from the VFM instruments) was available for each ASM-V data selected, to build a mirror L1b data set which we used to build twin models for comparison purposes and assessing model uncertainties (see sections 4 and 6 below).

This resulted in the selection of **612 360 scalar data** and **2 406 813 x 3 vector data**, distributed in time and latitude as illustrated in Figure 1.

3) Parent model parameterization:

The model parameterization follows that of Vigneron et al. (2021), itself an evolution of that of Hulot et al. (2015). It uses an approach similar to that used for the CHAOS-4 model (Olsen et al., 2014) to better account for temporal evolution over more than 10 years.

It involves a grand total of **10234** coefficients corresponding to:

- Time-varying internal field up to degree and order 13 (included), using order 6 B-splines with a 6 months knots separation.
This led to 26 splines and $26 \times 13 \times (13+2) = 5070$ coefficients
 - Static internal field between degree and order 14 (included) and degree and order 45 (included).
This led to an additional $45(45+2) - 13(13+2) = 1920$ coefficients
 - External field modeled as in Hulot et al. (2015, where details can be found):
 - Remote magnetospheric sources : $q_n^{0,\text{GSM}}$ in GSM frame, with $n=1,2 \rightarrow 2$ coefficients
 - Near magnetospheric ring current :
up to degree and order 2 in SM frame → 8 coefficients
 Δq estimated every 5 days for q_{10}
(748 time segments, → 748 coefficients)
 - Δq estimated every 30 days for q_{s11}
(127 time segments, → $2 \times 127 = 254$ coefficients)
- Leading to a total of $2+8+748+254 = 1012$ coefficients
- Euler angles (rotation between ASM and STR reference frames) estimated every 10 days for both satellites : 374/370 time segments for Alpha and Bravo
Leading to a total of $3 \times (374+370) = 2232$ coefficients

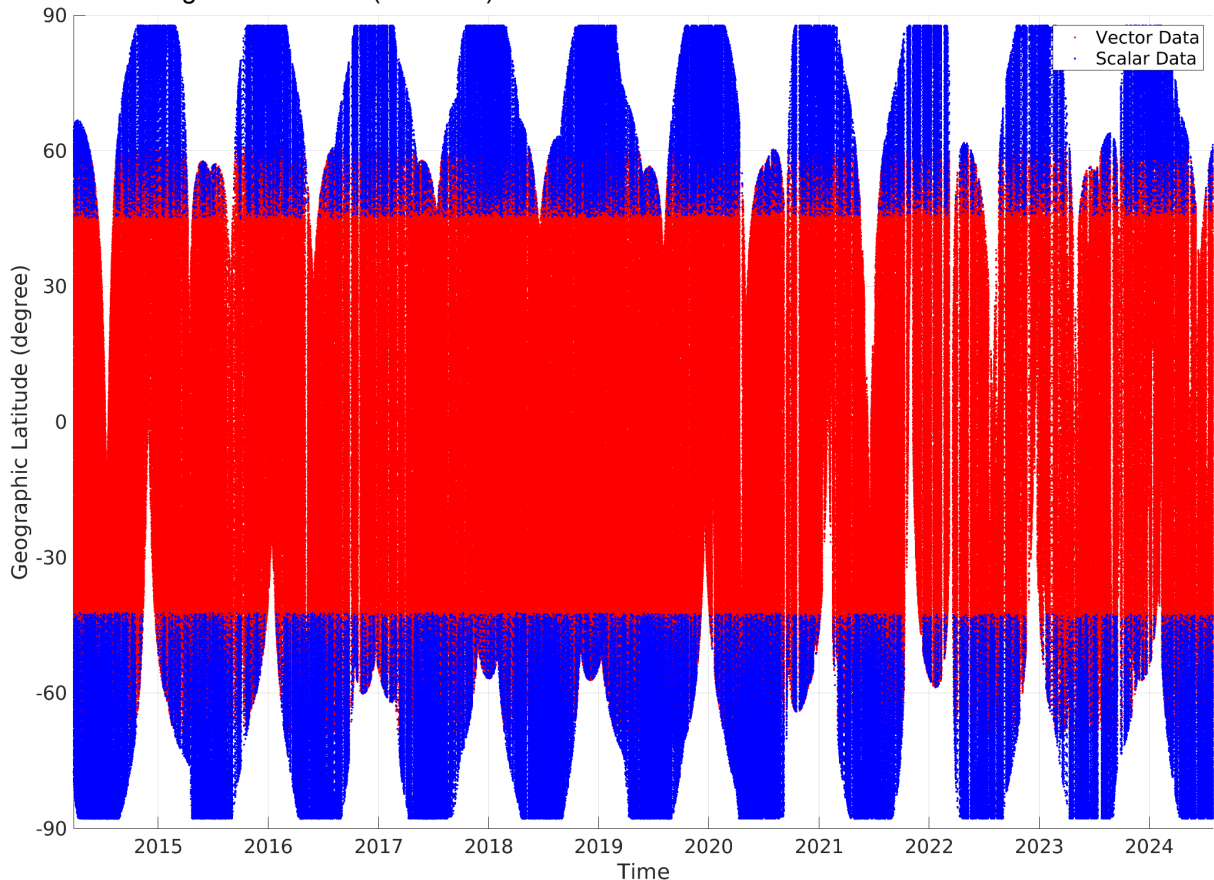


Figure 1: Data distribution as a function of time and latitude (blue: scalar data; red: vector data). Note the slightly less dense data coverage after 2020, due to ASM Burst mode sessions, when no ASM-V data is being acquired, more frequently occurring since that time (typically lasting one week per month on each Alpha and Bravo satellite).

4) Parent model optimization:

An initial parent model based on the ASM-V data was computed using the same approach as in Vigneron et al., (2021) by minimizing the mismatch between data and model prediction, using iteratively reweighted least-squares with Huber weights and temporal damping as in Olsen et al. (2014), but only using two damping parameters λ_2 and λ_3 :

- $\lambda_2 : \left| \frac{d^2 B_r}{dt^2} \right|$ constrained at beginning and end of dataset (namely March-2014 and July-2024) with the same damping value as for CHAOS-4 ($\lambda_2 = 10$)
- $\lambda_3 : \left| \frac{d^3 B_r}{dt^3} \right|$ integrated at the core surface and over the time coverage constrained with the same damping value as CHAOS-4 ($\lambda_3 = 0.33$ for all Gauss coefficients except for g_{10} where $\lambda_3=10$)

As in Hulot et al. (2015) and Vigneron et al. (2021), a geographical weight was introduced, proportional to $\sin(\theta)$ (where θ is the geographic colatitude), to balance the geographical sampling of data. Anisotropic magnetic errors due to attitude uncertainty were taken into account assuming an isotropic attitude error of 10 arcsecs (recall, indeed, that even isotropic attitude error produces anisotropic magnetic errors, see Holme and Bloxham (1996), the formalism of which we rely on). A priori data error variances were otherwise set to 2.2 nT for both scalar and vector data. The starting model used is a static model (CHAOS-4 up to degree and order 13 only for epoch 26/03/14), but this choice was found to not have any influence on the final model. A total of eight iterations were used, which was found to ensure convergence to within the accuracy required.

Resulting residual statistics are shown in Tables 1 and 2. A similar twin model was next built using the mirror Swarm L1b nominal data version 0602/0606 data set, with corresponding analogous statistics shown in Tables 3 and 4.

All these statistics are very comparable to those associated with the construction of the analogous ASM-V and twin parent models which we had produced in 2020 for the purpose of proposing a DGRF 2015 candidate model for IGRF13 (Vigneron et al., 2021). This suggests that we are on good tracks for building a DGRF 2020 candidate model of as high a quality as the DGRF 2015 candidate model we had proposed in 2020.

ASM-V SAT-A and SAT-B	# samples	residuals mean [nT]	residuals std [nT]	Huber Weight residuals mean [nT]	Huber Weight residuals std [nT]	Sum of weights
F (polar)	612360	0.69	7.41	-0.06	3.81	0.84
F and B_B	3019173	0.16	3.98	0.03	2.50	0.94
F and B_B low lat	2406813	0.02	2.43	0.05	2.10	0.96
B_B	2406813	0.02	2.43	0.05	2.10	0.96
B_r	2406813	-0.01	2.47	-0.01	2.19	0.88
B_theta	2406813	0.05	4.06	0.05	3.24	0.91
B_phi	2406813	-0.03	3.56	-0.01	2.86	0.90

Table 1: Residual statistics for all ASM-V data used to produce the ASM-V initial parent model (using the same convention as in Hulot et al., 2015 and Vigneron et al., 2021). B_B refers to vector residuals projected along the field direction; “Low lat” refers to data within (absolute) QD latitude 55°; F (polar) refers to scalar data above (absolute) QD latitude 55°.

ASM-V SAT-A	# samples	residuals mean [nT]	residuals std [nT]	Huber Weight residuals mean [nT]	Huber Weight residuals std [nT]	Sum of weights
F (polar)	302426	0.61	7.76	-0.14	3.94	0.83
F and B_B	1475747	0.14	4.15	0.01	2.56	0.93
F and B_B low lat	1173321	0.02	2.47	0.05	2.14	0.76
B_B	1173321	0.02	2.47	0.05	2.14	0.96
B_r	1173321	0.01	2.57	0.01	2.27	0.88
B_θ	1173321	0.03	4.08	0.02	3.27	0.91
B_φ	1173321	0.00	3.61	0.00	2.90	0.89

ASM-V SAT-B	# samples	residuals mean [nT]	residuals std [nT]	Huber Weight residuals mean [nT]	Huber Weight residuals std [nT]	Sum of weights
F (polar)	309934	0.77	7.05	0.02	3.68	0.85
F and B_B	1543426	0.17	3.81	0.04	2.44	0.94
F and B_B low lat	1233492	0.02	2.39	0.05	2.07	0.77
B_B	1233492	0.02	2.39	0.05	2.07	0.96
B_r	1233492	-0.04	2.36	-0.03	2.10	0.89
B_θ	1233492	0.06	4.04	0.08	3.20	0.91
B_φ	1233492	-0.05	3.52	-0.02	2.82	0.90

Table 2: Separate residual statistics for all Swarm Alpha (SAT-A, top Table) and Swarm Bravo (SAT-B, bottom Table) ASM-V data used to produce the ASM-V initial parent model.

VFM twin SAT-A and SAT-B	# samples	residuals mean [nT]	residuals std [nT]	Huber Weight residuals mean [nT]	Huber Weight residuals std [nT]	Sum of weights
F (polar)	612360	0.71	7.43	-0.05	3.82	0.84
F and B_B	3019173	0.14	3.97	0.01	2.48	0.94
F and B_B low lat	2406813	0.00	2.40	0.02	2.07	0.96
B_B	2406813	0.00	2.40	0.02	2.07	0.96
B_r	2406813	-0.01	1.79	-0.01	1.54	0.93
B_θ	2406813	0.00	3.44	0.01	2.78	0.94
B_φ	2406813	-0.03	3.05	0.00	2.45	0.93

Table 3: same as Table 1, but for all Swarm L1b nominal data version 0602/0606 used to produce the initial twin model.

VFM twin SAT-A	# samples	residuals mean [nT]	residuals std [nT]	Huber Weight residuals mean [nT]	Huber Weight residuals std [nT]	Sum of weights
F (polar)	302426	0.63	7.78	-0.13	3.96	0.83
F and B_B	1475747	0.11	4.14	-0.02	2.54	0.94
F and B_B low lat	1173321	-0.03	2.43	0.00	2.10	0.77
B_B	1173321	-0.03	2.43	0.00	2.10	0.96
B_r	1173321	0.03	1.75	0.03	1.57	0.93
B_θ	1173321	0.03	3.44	0.04	2.79	0.94
B_φ	1173321	-0.03	3.07	0.00	2.46	0.92

VFM twin SAT-B	# samples	residuals mean [nT]	residuals std [nT]	Huber Weight residuals mean [nT]	Huber Weight residuals std [nT]	Sum of weights
F (polar)	309934	0.79	7.06	0.04	3.69	0.85
F and B_B	1543426	0.17	3.81	0.04	2.43	0.94
F and B_B low lat	1233492	0.02	2.38	0.04	2.05	0.77
B_B	1233492	0.02	2.38	0.04	2.05	0.97
B_r	1233492	-0.05	1.83	-0.05	1.51	0.92
B_θ	1233492	-0.03	3.45	-0.01	2.77	0.94
B_φ	1233492	-0.04	3.03	0.00	2.45	0.93

Table 4: same as Table 2, but for all Swarm Alpha (SAT-A, top Table) and Swarm Bravo (SAT-B bottom Table) Swarm L1b nominal data version 0602/0606 used to produce the initial twin model..

Computing the difference between the predictions of our two initial parent models for epoch 2020 at Earth's surface confirms this first impression (Figures 2-4). Important to highlight, indeed, is that these maps are very comparable to the analogous maps we could produce in 2020 when comparing the two analogous parent models for epoch 2015. The largest signature, found in the radial component (Figure 2), is indeed very similar to the signature seen in Figure 4 of Vigneron et al. (2021). At the time, we speculated that this signature (testifying for some systematic disagreements between the ASM-V and nominal L1b data) could either be due to small distortions of the boom (mechanically linking the VFM and ASM instruments), to the fact that at the time the so-called dBSun perturbations (Tøffner-Clausen et al., 2016) were assumed to only affect the VFM instrument (and the correction therefore only applied to the nominal L1b data, and not to the ASM-V data), or to possible remaining unidentified ASM-V calibration issues. Figure 2, however, shows that applying the latest dBSun correction (now split into one perturbation affecting the VFM instrument, another affecting the ASM instrument as implemented in the production of the ASM-V and nominal L1b data used to recover our two initial parent models, recall section 2), does not remove this signature.

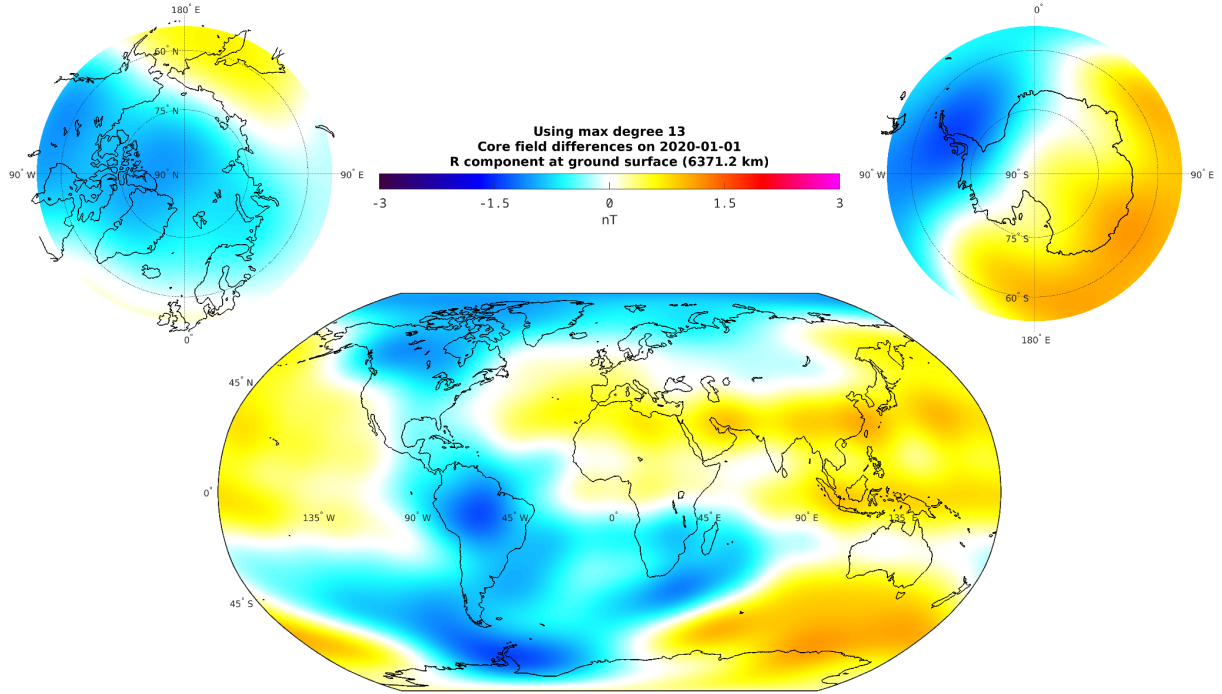


Figure 2: Radial component B_r of the difference between the predictions of the ASM-V initial parent model and its twin model for epoch 2020 at Earth's surface (up to degree and order 13; min = -1.424 nT, max = 1.149 nT, std = 0.606 nT).

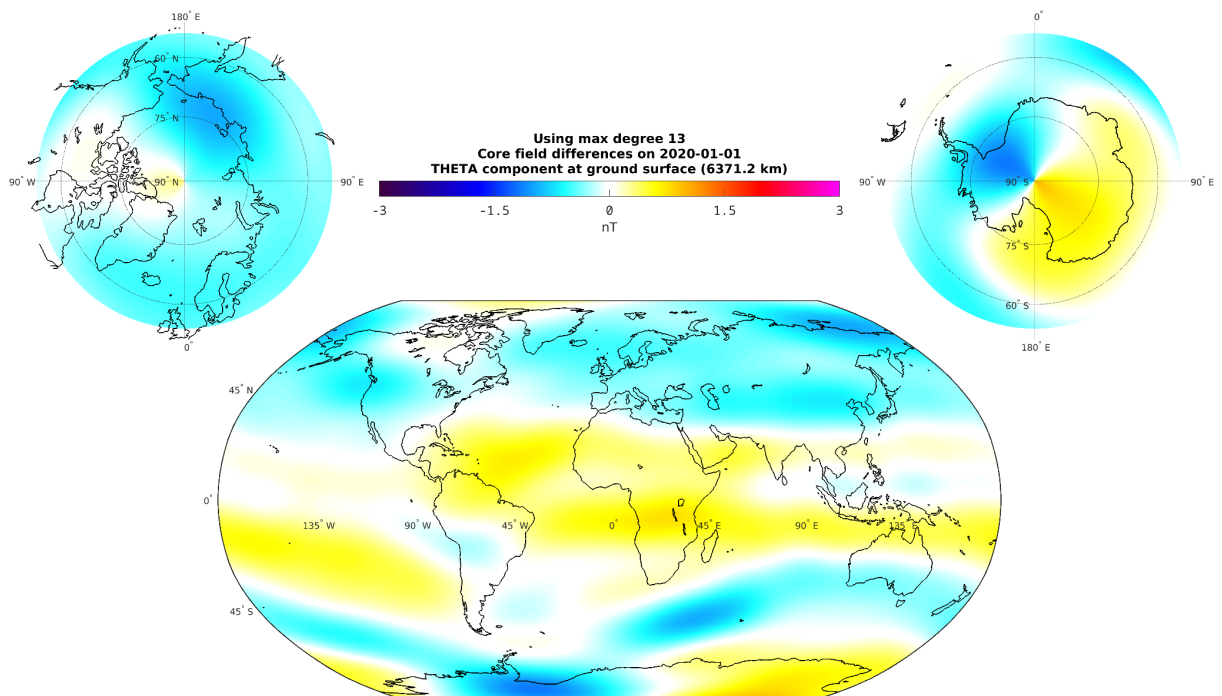


Figure 3: Latitudinal component B_θ of the difference between the predictions of the ASM-V initial parent model and its twin model for epoch 2020 at Earth's surface (up to degree and order 13; min = -1.177 nT, max = 0.988 nT, std = 0.380 nT).

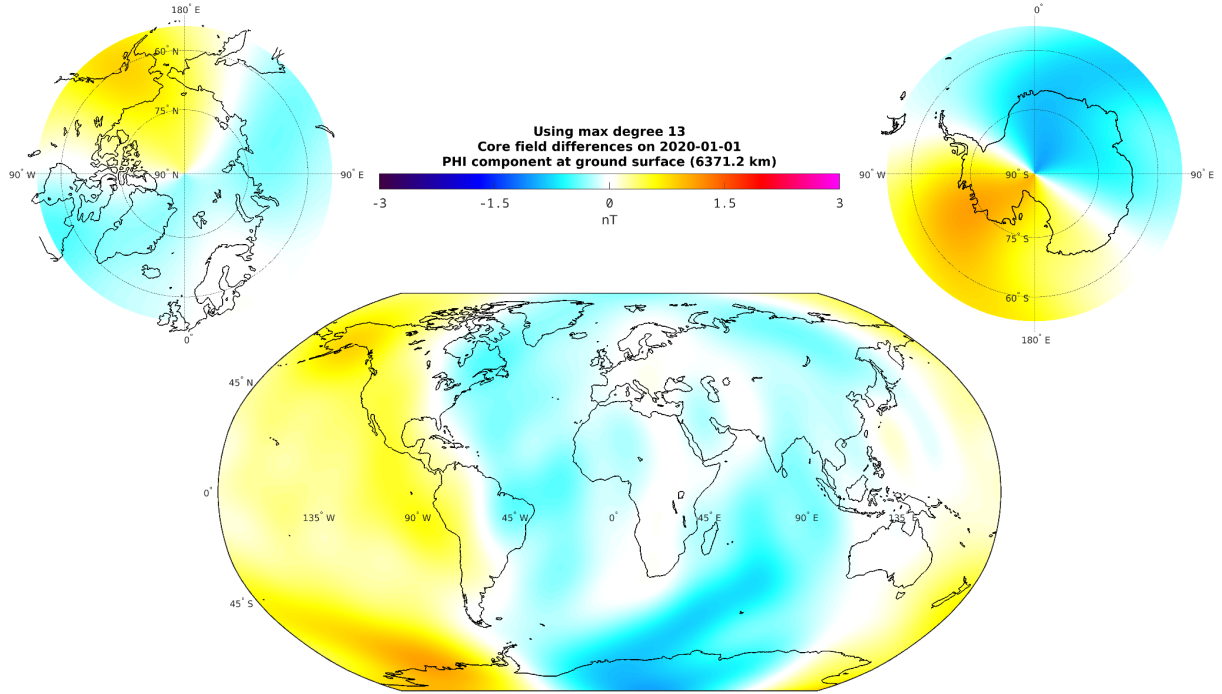


Figure 4: Longitudinal component B_ϕ of the difference between the predictions of the ASM-V initial parent model and its twin model for epoch 2020 at Earth's surface (up to degree and order 13; min = -0.992 nT, max = 1.116 nT, std = 0.383 nT).

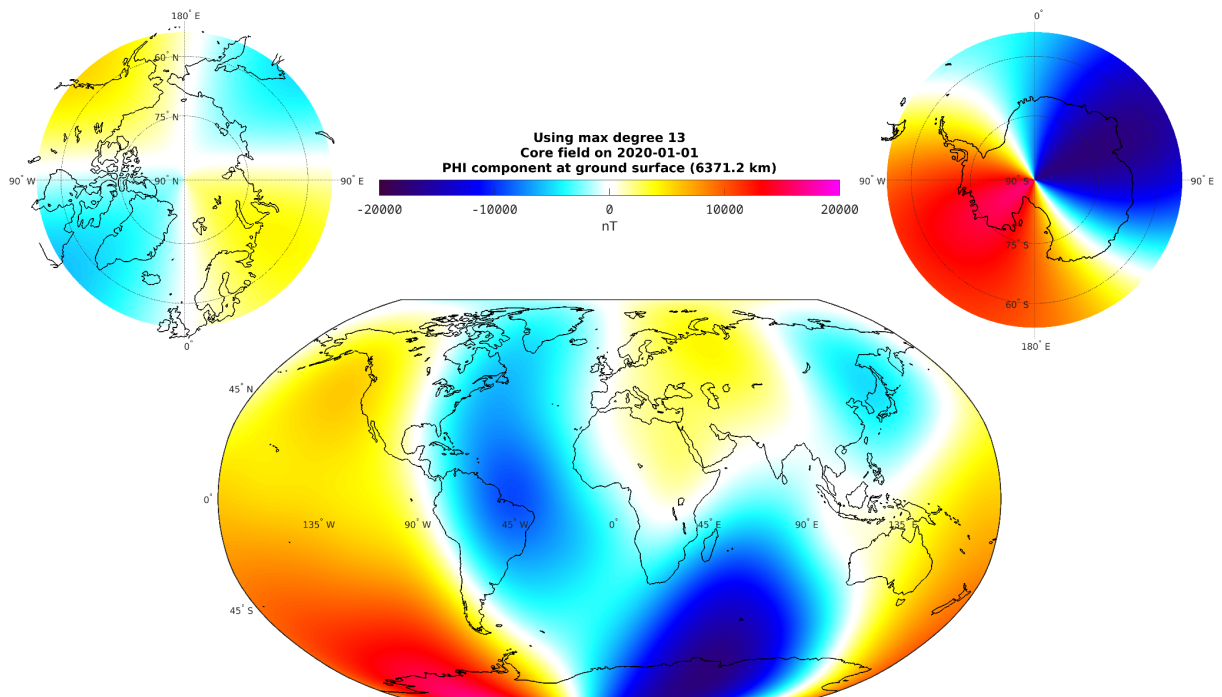


Figure 5: Longitudinal component B_ϕ of the field predicted by the initial twin model for epoch 2020 at Earth's surface (up to degree and order 13).

Thorough comparisons of these new ASM-V and nominal L1b data (not reported in this notice for the sake of brevity, but to be reported in the publication we intend to submit to the planned IGRF special issue) have now shown that the issue is in fact caused by a systematic disagreement between the Y components of the field measured by the ASM and VFM instruments, proportional to the Y component measured by the instruments (while no similar issue has been identified in the X and Z components). This clearly points at an issue equivalent to a remaining calibration issue on the Y component of either or both the ASM and VFM instruments.

Indeed, a careful look at Figures 4 and 5, which respectively show the difference between the longitudinal component B_{ϕ} predictions of the initial ASM-V parent model and its twin model, and the longitudinal component B_{ϕ} predictions of the twin model, both for epoch 2020 at Earth's surface, clearly points at a signature proportional to the signal predicted. Bearing in mind that the Y components of the ASM and VFM instruments are essentially aligned with the longitudinal component B_{ϕ} , this again suggests that compared to the nominal L1b data (from the VFM instrument) the ASM-V data (from the ASM instrument) tends to overestimate the Y component of the field measured, which is next reflected in the difference between the longitudinal component B_{ϕ} predictions of the initial ASM-V parent and twin models.

What Figures 4 and 5, and direct comparison of ASM-V and nominal L1b data, cannot tell however, is by how much each instrument could be affected by this apparent Y component calibration issue. We therefore designed a method to answer this question independently for each instrument and satellite. This method is based on analyzing the Y component residuals between the data used (e.g. ASM-V data) and the prediction of the model built from these data (e.g. the initial ASM-V parent model). The details of this method will also be provided in the publication we intend to submit to the planned IGRF special issue. Here, we only provide the “post-calibration” results of this analysis.

The method first allows us to infer the optimal rescaling factor to apply to the Y component on each instrument and each satellite. These factors are provided in Table 5 below. Indeed, and as can be seen, ASM-V data need to be rescaled for slightly overestimating the Y component (on both Swarm Alpha and Bravo), while the L1b nominal data version 0602/0606 need to be rescaled for slightly (and significantly less) underestimating this component. Note that both rescalings work in opposite directions and that similar rescaling factors apply to both Alpha and Bravo.

Since rescaling the Y component does slightly affect the modulus of the vector data (not much, as the Y component is never the dominant component), we next further renormalize the new vector data (all three X, Y and Z components) for the modulus of the renormalized vector to exactly match the independent scalar field value also provided with each data set.

These new “post-calibrated” ASM-V and Swarm L1b nominal data sets, are next used to recompute new (and final) parent ASM-V and twin Swarm L1b nominal data models. For these computations, we use exactly the same parameters and codes as those used for the initial parent field models above. Note also that we do not use any new or additional data selection criteria. We simply apply the above “post-calibration” scheme to the previously selected data sets.

Residual statistics for the final parent ASM-V model are shown in Tables 6 and 7 (analogous to Tables 1 and 2 for the initial parent ASM-V model). Those for the final twin Swarm L1b nominal data model are shown in Tables 8 and 9 (analogous to Tables 3 and 4 for the initial twin Swarm L1b nominal data model).

$\text{new_By} = a * \text{By}$	Rescaling factor (“a” parameter) for SAT-A	Rescaling factor (“a” parameter) for SAT-B
ASM-V data	0.9998706	0.9998647
VFM data	1.0000610	1.0000496

Table 5: Rescaling factors used to post-calibrate the Y components of the ASM-V data (first line) and Swarm L1b nominal data version 0602/0606 (second line) for Swarm Alpha (first column) and Swarm Bravo (second column)

ASM-V SAT-A and SAT-B	# samples	residuals mean [nT]	residuals std [nT]	Huber Weight residuals mean [nT]	Huber Weight residuals std [nT]	Sum of weights
F (polar)	612360	0.68	7.41	-0.06	3.81	0.84
F and B_B	3019173	0.14	3.97	0.01	2.50	0.94
F and B_B low lat	2406813	0.00	2.42	0.03	2.10	0.96
B_B	2406813	0.00	2.42	0.03	2.10	0.96
B_r	2406813	-0.02	2.46	-0.02	2.18	0.88
B_θ	2406813	0.01	4.06	0.02	3.24	0.91
B_φ	2406813	-0.03	3.53	0.00	2.83	0.90

Table 6: Residual statistics for all post-calibrated ASM-V data used to produce the ASM-V final parent model (using the same convention as in Hulot et al., 2015 and Vigneron et al., 2021). B_B refers to vector residuals projected along the field direction; “Low lat” refers to data within (absolute) QD latitude 55°; F (polar) refers to scalar data above (absolute) QD latitude 55°.

ASM-V SAT-A	# samples	residuals mean [nT]	residuals std [nT]	Huber Weight residuals mean [nT]	Huber Weight residuals std [nT]	Sum of weights
F (polar)	302426	0.61	7.76	-0.14	3.95	0.83
F and B_B	1475747	0.13	4.14	0.00	2.56	0.94
F and B_B low lat	1173321	0.01	2.46	0.03	2.13	0.76
B_B	1173321	0.01	2.46	0.03	2.13	0.96
B_r	1173321	0.01	2.57	0.01	2.27	0.88
B_θ	1173321	0.00	4.09	0.00	3.28	0.91
B_φ	1173321	-0.01	3.57	0.00	2.87	0.89

ASM-V SAT-B	# samples	residuals mean [nT]	residuals std [nT]	Huber Weight residuals mean [nT]	Huber Weight residuals std [nT]	Sum of weights
F (polar)	309934	0.76	7.05	0.02	3.68	0.85
F and B_B	1543426	0.15	3.81	0.03	2.44	0.94
F and B_B low lat	1233492	0.00	2.38	0.03	2.06	0.77
B_B	1233492	0.00	2.38	0.03	2.06	0.97
B_r	1233492	-0.04	2.36	-0.04	2.10	0.89
B_θ	1233492	0.03	4.04	0.05	3.20	0.91
B_φ	1233492	-0.06	3.48	-0.01	2.79	0.90

Table 7: Separate residual statistics for all Swarm Alpha (SAT-A, top Table) and Swarm Bravo (SAT-B, bottom Table) post-calibrated ASM-V data used to produce the ASM-V final parent model.

VFM twin SAT-A and SAT-B	# samples	residuals mean [nT]	residuals std [nT]	Huber Weight residuals mean [nT]	Huber Weight residuals std [nT]	Sum of weights
F (polar)	612360	0.72	7.42	-0.04	3.81	0.84
F and B_B	3019173	0.15	3.97	0.02	2.48	0.94
F and B_B low lat	2406813	0.00	2.39	0.03	2.07	0.96
B_B	2406813	0.00	2.39	0.03	2.07	0.96
B_r	2406813	-0.01	1.78	0.00	1.54	0.93
B_θ	2406813	0.01	3.44	0.03	2.77	0.94
B_φ	2406813	-0.03	3.05	0.00	2.46	0.93

Table 8: same as Table 6, but for all post-calibrated Swarm L1b nominal data version 0602/0606 used to produce the final twin model.

VFM twin SAT-A	# samples	residuals mean [nT]	residuals std [nT]	Huber Weight residuals mean [nT]	Huber Weight residuals std [nT]	Sum of weights
F (polar)	302426	0.64	7.78	-0.12	3.95	0.83
F and B_B	1475747	0.13	4.13	-0.01	2.54	0.94
F and B_B low lat	1173321	0.00	2.42	0.02	2.10	0.77
B_B	1173321	0.00	2.42	0.02	2.10	0.96
B_r	1173321	0.01	1.75	0.01	1.56	0.93
B_θ	1173321	0.03	3.43	0.05	2.78	0.94
B_φ	1173321	-0.03	3.07	0.00	2.46	0.92

VFM twin SAT-B	# samples	residuals mean [nT]	residuals std [nT]	Huber Weight residuals mean [nT]	Huber Weight residuals std [nT]	Sum of weights
F (polar)	309934	0.80	7.06	0.04	3.68	0.85
F and B_B	1543426	0.17	3.80	0.04	2.42	0.94
F and B_B low lat	1233492	0.01	2.36	0.04	2.04	0.77
B_B	1233492	0.01	2.36	0.04	2.04	0.97
B_r	1233492	-0.02	1.80	-0.02	1.51	0.92
B_θ	1233492	0.00	3.44	0.01	2.76	0.94
B_φ	1233492	-0.03	3.03	0.00	2.45	0.93

Table 9: same as Table 7, but for all Swarm Alpha (SAT-A, top Table) and Swarm Bravo (SAT-B, bottom Table) post-calibrated Swarm L1b nominal data version 0602/0606 used to produce the final twin model.

Comparing Tables 6-7 with Tables 1-2 shows that statistics for the post-calibrated ASM-V data hardly differ from those of the initial ASM-V data. Comparing Tables 8-9 with Tables 3-4 shows that the same holds for the post-calibrated Swarm L1b nominal data version 0602/0606. This is encouraging.

Even more encouraging, however, is the result of the comparison of the predictions from the ASM-V final parent model and its twin final model. The difference between the predictions of these two final parent models for epoch 2020 at Earth's surface is shown in Figures 6-8 for the three B_r , B_θ and B_ϕ components.

Comparing Figures 8 and 4 first shows that differences in the predicted B_ϕ components are now much weaker, with hardly any signature left. This is good news, and confirms that the main reason for the original signature seen in Figure 4 was indeed the Y component calibration issue we identified and corrected for. To a large extent, this of course is what one would have expected, given that the Y component of the magnetic field measured by the ASM and VFM instruments is along the B_ϕ component predicted by the models.

Even more encouraging, however, is the fact that this improvement in the B_ϕ component did not come at the cost of an increase in the differences in the B_r and B_θ components.

Quite the contrary ! Comparing Figures 7 and 3 clearly shows an overall decrease in the disagreements in the B_θ component, while comparing Figures 6 and 2 reveals an even greater overall decrease in the disagreements in the B_r component. This we interpret as a sign that as a result of being potential field models, both the ASM-V initial parent model and its twin model had to accommodate the over (and under) calibrated Y components by also introducing spurious signals in both the B_θ and B_r components, both of which have been removed in the ASM-V final parent model and its twin model by the post-calibration strategy we introduced.

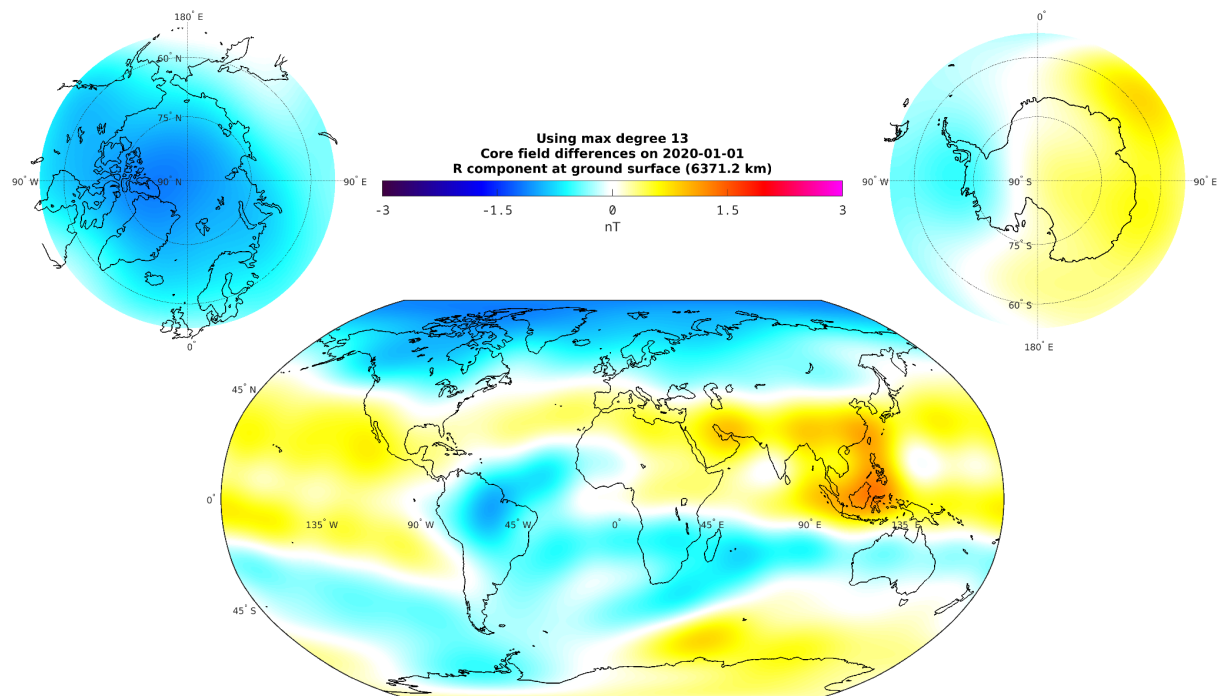


Figure 6: Radial component B_r of the difference between the predictions of the ASM-V final parent model and its twin model for epoch 2020 at Earth's surface (up to degree and order 13; min = -1.165 nT, max = 1.341 nT, std = 0.497 nT).

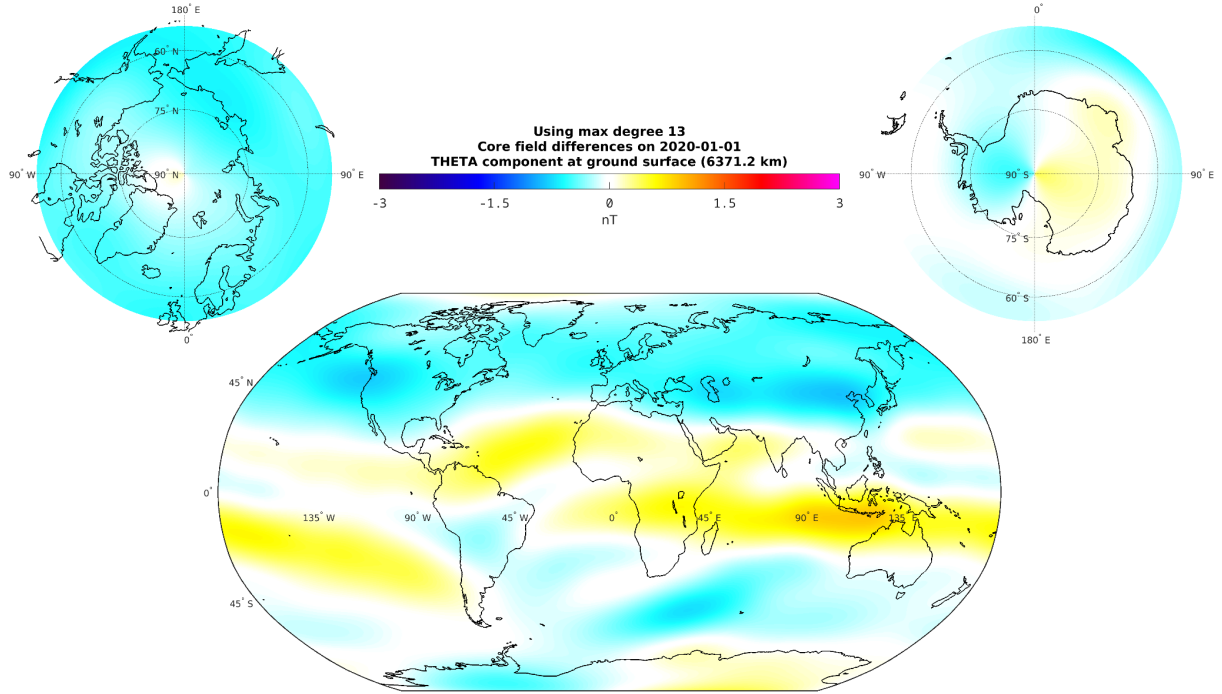


Figure 7: Latitudinal component B_θ of the difference between the predictions of the ASM-V final parent model and its twin model for epoch 2020 at Earth's surface (up to degree and order 13; min = -0.864 nT, max = 0.909 nT, std = 0.317 nT).

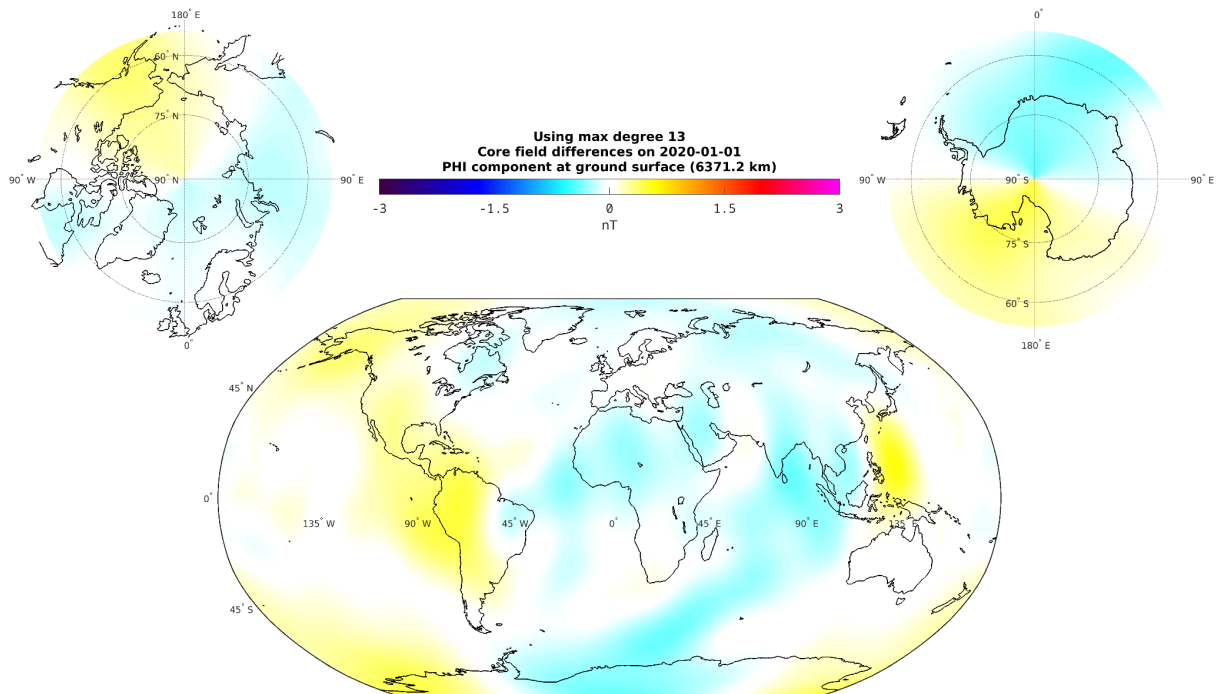


Figure 8: Longitudinal component B_ϕ of the difference between the predictions of the ASM-V final parent model and its twin model for epoch 2020 at Earth's surface (up to degree and order 13; min = -0.432 nT, max = 0.577 nT, std = 0.178 nT).

5) DGRF 2020 candidate model generation

The above very encouraging results prompt us to rely on our ASM-V final parent model, entirely based on (post-calibrated) ASM-V data, to propose our final DGRF 2020 candidate model.

This final DGRF 2020 candidate model is simply computed from our ASM-V final parent model for epoch 2020.0 and truncated at degree 13.

6) Computation of realistic uncertainties on each Gauss coefficient

To assess “realistic” uncertainties on each Gauss coefficient, we rely on the same strategy as the one previously used by (Vigneron et al., 2021), when we proposed our DGRF 2015 candidate model. This strategy only assesses uncertainties produced by the quality of the data (i.e., it does not assess the uncertainties due to the choice of the modeling strategy, choice of data selection criteria and choice of parameters for the inversion, such as damping parameters, etc...). These uncertainties should thus be viewed as a lower bound indication of the “real” uncertainties.

We first split the post-calibrated ASM-V data set in two: ordering and numbering data as a function of time, every even number data is put in sub-dataset ASMV-1, every odd data is put in sub-dataset ASMV-2. Likewise, the twin VFM data set (post-calibrated Swarm L1b nominal data, version 0602/0606) is split in two VFM-1 and VFM-2 datasets (the time distribution of VFM-1/2 data matching that of ASMV-1/2). A model is next computed from each sub-dataset, using the same parameters as the final parent (and twin) model, leading to four models: ASMV-1 and VFM-1 (sharing the same even number data distribution) and ASMV_2 and VFM_2 (sharing the same odd number data distribution). For each Gauss coefficients, the values A1 (from ASMV_1), A2 (from ASMV-2), V1 (from VFM1) and V2 (from VFM2) are next used to compute the quantity $E = \sqrt{[1/2 \times \{(A1-V2)x(A1-V2) + (A2-V1)x(A2-V1)\}]}$, which we assign as one sigma type of error on the corresponding Gauss coefficient. These values are provided as s_g (for the g coefficient) and s_h (for the h coefficient) with 2 significant digits.

Note that this technique only provides an estimate of variances and ignores possible cross-correlations in errors between Gauss coefficients. But it can also be used to compute the geographical distribution of errors (one sigma type) predicted for local quantities, such as B_r values (now using local values of the predicted Br by the same four models, using the same formula $E = \sqrt{[1/2 \times \{(A1-V2)x(A1-V2) + (A2-V1)x(A2-V1)\}]}$). Figure 9 provides a map of this predicted error.

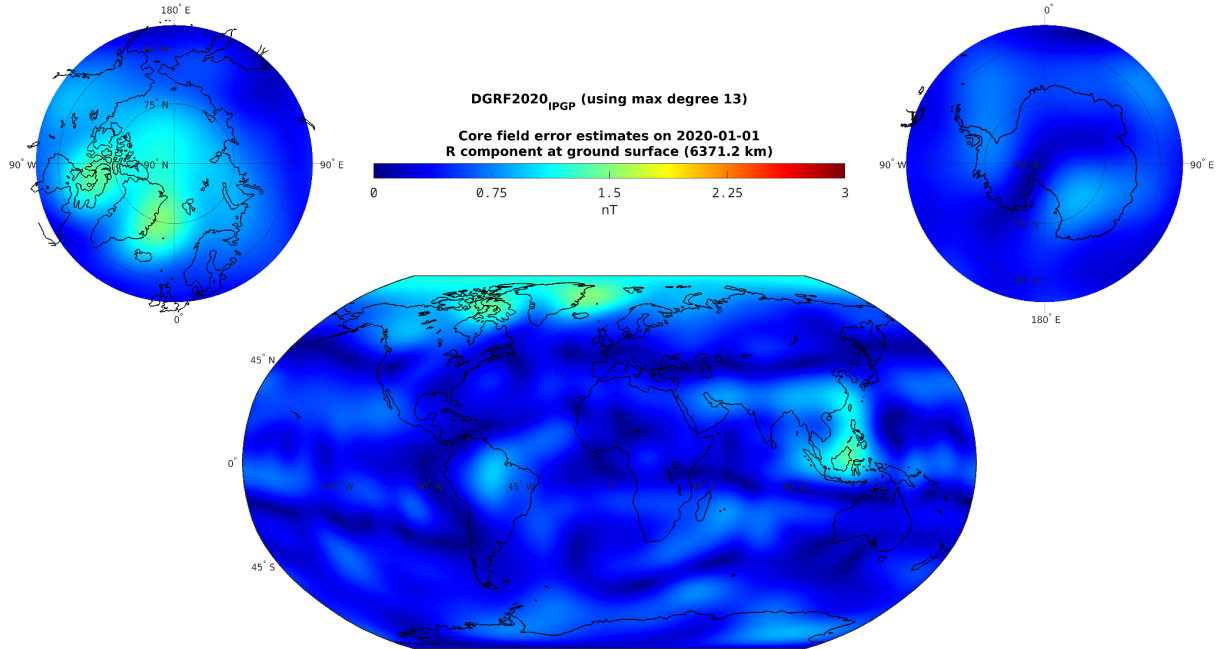


Figure 9: Local errors (one sigma type) computed using the technique described in the text for the radial component B_r at Earth's surface.

Note also that, as one would have expected, geographical locations of large errors in Figure 9 decently match the location of large differences between the B_r component predictions of the ASM-V final parent model and its twin model for epoch 2020 at Earth's surface (Figure 6).

7) Initial Validation

To provide an initial assessment of the quality of the final DGRF 2020 candidate model we produced, we simply compared this model to the CHAOS-7.18 model for epoch 2020.0. This CHAOS-7.18 model was computed by DTU only using original (no post-calibration of the type we introduced) 0602/0606 L1b Swarm data, plus data from other missions as well as data from ground observatories. The modeling is similar in spirit (also using splines, etc...) to the modeling technique we used, but differs in many details (choice of parameters, etc...), and also involves the use of gradient data (see Finlay et al., 2020). Figure 10 illustrates the geographical distribution of the absolute value of the difference in the B_r values predicted by our final DGRF 2020 candidate model and CHAOS-7.18. It is interesting to see that these differences have many similarities with the errors predicted by the technique described in section 6 (and shown in Figure 9) and are reasonably comparable in magnitude, lending some credit to the estimate of uncertainties we provide for each Gauss coefficient.

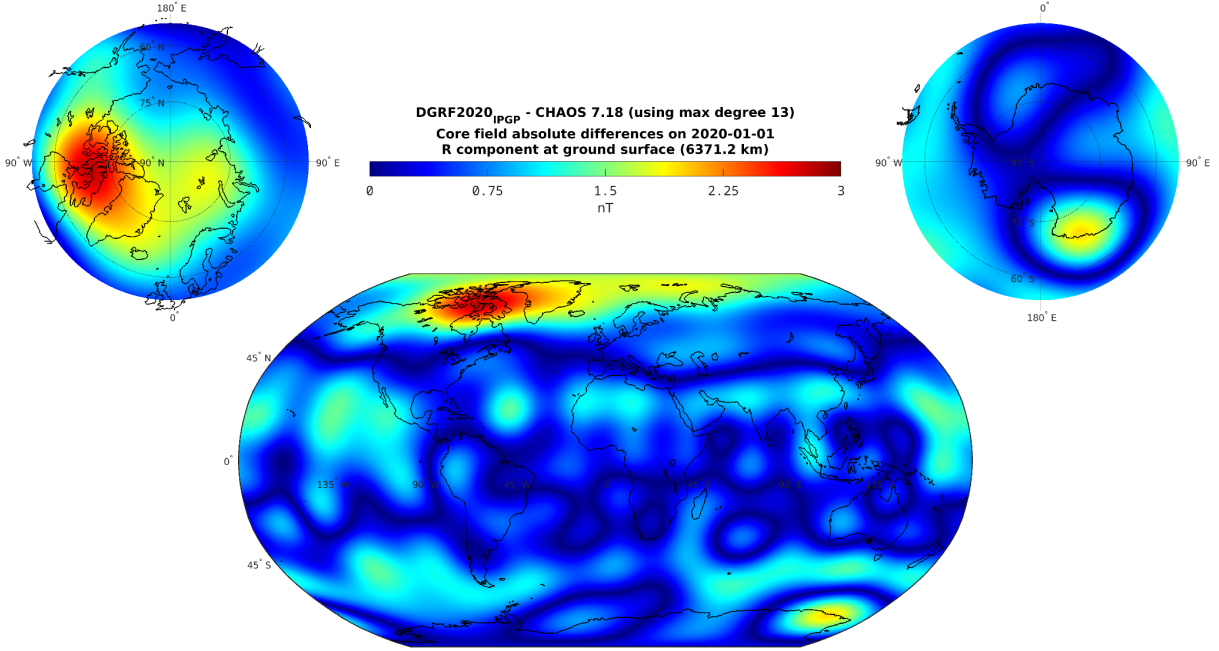


Figure 10: Absolute value of the difference in the B_r values predicted by our final DGRF 2020 candidate model and CHAOS-7.18 at Earth's surface.

We also computed the Lowes-Mauersberger spectrum of the difference between our final DGRF 2020 candidate model and the CHAOS 7.18 model at epoch 2020 and compared this spectrum to a number of relevant spectra. Figure 11 shows that this spectrum (red dashed line) is below (in particular for degree 1) the analogous spectrum of the difference between the ASM-V initial parent model (initial DGRF 2020 candidate model) and the CHAOS 7.18 model for epoch 2020 (green dashed line). This shows that the strategy we used for post-calibrating the ASM-V data to produce our final DRGF 2020 candidate model did improve the agreement of our model with the CHAOS 7.18 model. Worth further pointing out is that this is true, despite the fact that the CHAOS 7.18 model relied on the original 0602/0606 L1b Swarm data, and not on the post-calibrated 0602/0606 L1b Swarm data, which we used to compute the twin model of our final DGRF 2020 candidate model. This is in line with the fact that the post-processing we used implied a stronger post-calibration of the ASM-V data than of the 0602/0606 L1b Swarm data (recall Table 5).

The benefit of post-calibrating both ASM-V data and 0602/0606 L1b Swarm data, which we already illustrated through the comparisons of Figures 6-8 with Figures 2-4, can nevertheless also be seen through the comparison of the spectrum of the difference between our final DGRF 2020 candidate model and its twin model computed from post-calibrated VFM Swarm L1b nominal data version 0602/0606 data (black dashed line) with the spectrum of the difference between the ASM-V initial parent model (initial DGRF 2020 candidate model) and its twin model at epoch 2020 (blue dashed line). The former spectrum again lies below the latter, particularly for degrees 1 and 6. Finally, we note that both these spectra are very comparable in magnitude to the spectrum of the difference between our final DGRF 2020 candidate model and the CHAOS 7.18 model at epoch 2020, itself on the very low side of the spectra of differences between previously published DGRF 2015 candidate models and the finally adopted DRGF 2015 model, as illustrated in Figure 1 of Alken et al. (2021).

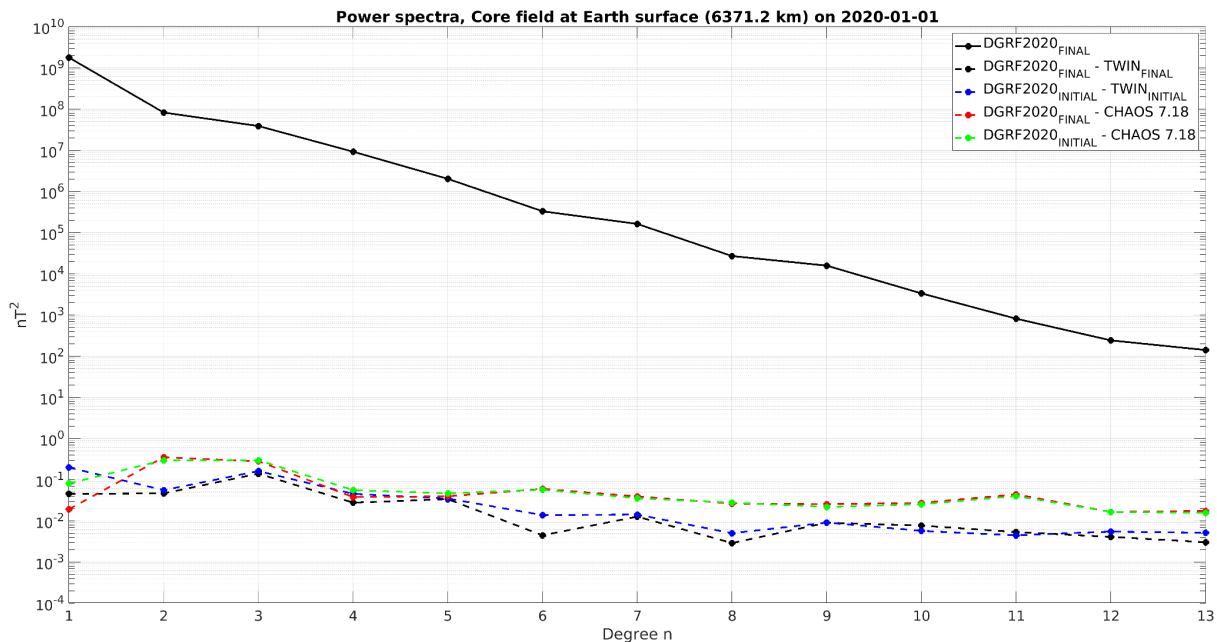


Figure 11: Spectra of our final DGRF 2020 candidate model (black solid line), of the difference between our final DGRF 2020 candidate model and its twin model computed from post-calibrated VFM Swarm L1b nominal data version 0602/0606 data (black dashed line), of the difference between the ASM-V initial parent model (initial DGRF2020 candidate model) and its twin model computed from VFM Swarm L1b nominal data version 0602/0606 data at epoch 2020 (blue dashed line), of the difference between our final DGRF 2020 candidate model and the CHAOS 7.18 model at epoch 2020 (red dashed line), and of the difference between the ASM-V initial parent model (initial DGRF2020 candidate model) and the CHAOS 7.18 model at epoch 2020 (green dashed line), all at Earth's surface.

8) Conclusion

We therefore conclude that our final DGRF 2020 candidate model entirely based on post-calibrated ASM-V data is a particularly valuable candidate for contribution to the final DGRF 2020 model.

9) References

Alken, P., Thébault, E., Beggan, C.D., Aubert, J., Baerenzung, J., Brown, W.J., Califf, S., Chulliat, A., Cox, G.A., Finlay, C.C., Fournier, A., Gillet, N., Hammer, M.D., Holschneider, M., Hulot, G., Korte, M., Lesur, V., Livermore, P.W., Lowes, F.J., MacMillan, S., Nair, M., Olsen, N., Ropp, G., Rother M., Schnepf, N.R., Stolle, C., Toh, H., Vervelidou, F., Vigneron, P., Wardinski, I., Evaluation of candidate models for the 13th generation of the International Geomagnetic Reference Field, *Earth Planets Space*, 73 : 48, <https://doi.org/10.1186/s40623-020-01281-4>, 2021.

Finlay, C.C., Kloss, C., Olsen, N. et al, The CHAOS-7 geomagnetic field model and observed changes in the South Atlantic Anomaly. *Earth Planets Space* 72, 156, <https://doi.org/10.1186/s40623-020-01252-9> , 2020. (For the CHAOS-7.18 version of this model, see <http://www.spacecenter.dk/files/magnetic-models/CHAOS-7/>).

Holme, R., and J. Bloxham, The treatment of attitude errors in satellite geomagnetic data, *Phys. Earth Planet. Inter.*, 98, 221–233, [http://dx.doi.org/10.1016/S0031-9201\(96\)03189-5](http://dx.doi.org/10.1016/S0031-9201(96)03189-5), 1996.

Hulot, G., Vigneron, P., Léger, J.-M., Fratter, I., Olsen, N., Jager, T., Bertrand, F., Brocco, L., Sirol, O., Lalanne, X., Boness, A., Cattin, V., Swarm's absolute magnetometer experimental vector mode, an innovative capability for space magnetometry, *Geophys. Res. Lett.*, 42,

<https://doi.org/10.1002/2014GL062700>, 2015.

Léger, J.M., Jager, T., Bertrand, F., Hulot G., Brocco, L., Vigneron, P., Lalanne, X., Chulliat, A., Fratter, I., In flight performance of the Absolute Scalar Magnetometer vector mode on board the Swarm satellites, *Earth Planets Space*, 67 : 57, <https://doi.org/10.1186/s40623-015-0231-1>, 2015.

Olsen, N., H. Lühr, C. C. Finlay, T. J. Sabaka, I. Michaelis, J. Rauberg, and L. Tøffner-Clausen, The CHAOS-4 geomagnetic field model, *Geophys. J. Int.*, 197, 815–827, <http://dx.doi.org/10.1093/gji/ggu033>, 2014.

Tøffner-Clausen, L., Lesur, V., Olsen, N., Finlay, C.C., In-flight scalar calibration and characterisation of the Swarm magnetometry package, *Earth, Planets and Space*, 68 :129, <https://doi.org/10.1186/s40623-016-0501-6>, 2016.

Vigneron, P., Hulot, G., Léger, JM. et al., Using improved Swarm's experimental absolute vector mode data to produce a candidate Definitive Geomagnetic Reference Field (DGRF) 2015.0 model, *Earth Planets Space* 73 : 197, <https://doi.org/10.1186/s40623-021-01529-7>, 2021.